A Comparative Study of Harmonic and Inter-Harmonic Detection Using Parallel- and Cascade-Connected Nonlinear Limit Cycle Oscillators

Erick Vazquez, and César Fernando Méndez-Barrios

***Abstract*—The accurate detection of harmonics and inter-harmonics is critical for power quality monitoring, yet challenging due to the complex, multi-component nature of electrical signals. This paper investigates and compares two detection methodologies based on networks of nonlinear Limit Cycle Oscillators (LCOs). A systematic performance evaluation assesses the ability of both parallel- and cascade-connected LCO structures to precisely estimate the frequency, magnitude, and phase of individual harmonic and inter-harmonic components. The findings, validated through experimental tests, highlight the comparative advantages and limitations of each architecture, providing practical insights for their application in enhancing energy efficiency within power systems.**

Link to graphical and video abstracts, and to code:
https://latamt.ieeer9.org/index.php/transactions/article/view/11047

***Index Terms*—Harmonic detection, Inter-harmonic detection, Limit Cycle Oscillators, Frequency locked loop.**

I. Introduction

THE growing integration of Distributed Energy Resources (DERs) and nonlinear loads into electrical distribution systems has introduced a vast range of disturbances across a broad frequency spectrum [1]–[6]. Among these, harmonics and inter-harmonics –defined as integer and non-integer multiples of the fundamental frequency, respectively – have become increasingly prevalent [7], [8]. These distortions are primarily caused by non-linear loads, including Personal Computers voltage sources, arc kiln, electronic ballasts, L.E.D. lighting, and, more recently, electric vehicle fast-charging stations [1], [3], [9]–[11]. Additionally, transformers, PV inverters, and rectifiers are significant contributors to harmonic generation [4], [6], [12], [13]. The proliferation of such loads, especially those with electronic interfaces, has significantly degraded power quality, particularly for consumers on adjacent feeders [14].

The negative outcome of harmonics and inter-harmonics on power systems are well-documented and wide-ranging [15]. These include equipment malfunction, reduced measurement accuracy, and compromised operation of critical infrastructure like phasor measurement units (PMUs) and SCADA systems [3]. Further consequences encompass voltage fluctuations, unintended thyristor switching, conductor overheating, and accelerated aging of induction motors [16]. From a dynamic perspective, these disturbances can be dangerously amplified when their frequencies coincide with grid resonances [17], [18]. This is a critical concern in weak distribution networks with high renewable penetration, where even low-amplitude inter-harmonics can trigger subsynchronous oscillations [19], [20]. Such issues, including overvoltages and increased losses, motivate the development of effective mitigation strategies [12], [13].

According to the United Nations Sustainable Development Goals for Latin America, enhancing energy efficiency represents a crucial pathway toward decarbonization. Since the energy sector is the leading driver of climate change, responsible for approximately 73 to 76 percent of global greenhouse gas emissions when accounting for energy supply alongside transport, industry, and buildings, improving efficiency directly contributes to reducing the global carbon footprint. [21]. Therefore, accurate and timely estimation of harmonic and inter-harmonic components is essential for improving energy efficiency.

Consequently, detection methods are broadly categorized as frame-based or recursive (parametric) [22]. Frame-based techniques, such as the Fast Fourier Transform (FFT), ESPRIT, MUSIC, and Prony-based methods, operate on data blocks and assume steady-state conditions [22], [23]. While well-established and incorporated into standards like IEEE 519-2014 [24], these methods are prone to spectral leakage, particularly from the picket-fence effect, which is exacerbated by inter-harmonics and off-nominal frequencies [2], [25]. Adaptive techniques like the Short-Time Fourier Transform (STFT) or sliding-window versions of ESPRIT and MUSIC can alleviate these issues but often at the cost of increased computational complexity and a continued need for synchronization mechanisms like Phase-Locked Loops (PLLs) [26].

In contrast, recursive methods, such as those based on ADALINE, Kalman filters, and PLLs, update model parameters continuously using incoming measurements [27]. These approaches are well-suited for tracking time-varying signals and offer rapid estimation. However, their performance is highly dependent on the accuracy of the underlying model

The associate editor coordinating the review of this manuscript and approving it for publication was José Miguel Sosa (*Corresponding author: Erick Vazquez).*

This paper was funded by the Secretariat of Science, Humanities, Technology and Innovation of Mexico under grant 423695.

Erick Vazquez, and C. F. Méndez-Barrios are with the Research and Postgraduate Studies Center of the Faculty of Engineering of the Autonomous University of San Luis Potosí, Mexico (e-mails: erick.vazquez@upslp.edu.mx, and fernando.barrios@uaslp.mx).

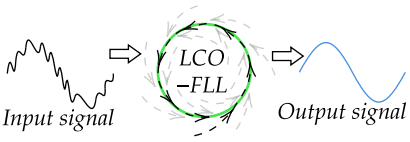


Fig. 1. LCO-FLL unit to find frequencies and phases of polluted signals.

and can degrade significantly in the presence of unmodeled dynamics or disturbances.

Recently, techniques based on nonlinear oscillators have emerged as promising alternatives for harmonic detection and synchronization [28]–[30]. Among these, the Limit Cycle Oscillator (LCO), particularly in its circular form, is notable for its inherent circular symmetry, which produces pure sinusoidal trajectories and offers robustness against frequency variations and disturbances [30]. However, the standard LCO lacks inherent frequency adaptability. To address this, Frequency-Locked Loops (FLLs) have been integrated with LCOs, providing a computationally simple mechanism for real-time frequency tracking without requiring phase angles or trigonometric functions [31]–[33]. This LCO-FLL combination creates a robust, adaptive unit well-suited for dynamic power system environments [34] to track frequencies and phases of polluted signals, as it is shown in Fig. 1.

This article provides a comparative case study of two distinct interconnection strategies for LCO-FLL-based algorithms to detect harmonics and inter-harmonics: a cascade (series) configuration and a parallel configuration. The theoretical frameworks for both the cascaded and parallel LCO-FLL structures are developed and compared. Subsequently, the performance of both detector architectures is validated and compared through experimental tests using power inverters, with a detailed discussion of their respective advantages and disadvantages.

The main contributions of this work can be summarized as follows:

- Enhancement of the proposed topologies, with a redesigned parallel configuration in which each block is implemented as a fully integrated LCO-FLL structure, rather than solely LCO blocks for harmonic detection as in [35].
- Extension of the architecture's capabilities to detect both harmonic and inter-harmonic components.
- Configuration of input/output interfaces to enable experimental comparison, moving beyond the simulation-only approaches reported in [35], [36].
- Execution of the experimental implementation, often regarded as one of the most challenging aspects of the overall work.

The remaining part of the paper is organized as follows: Section II introduces the core synchronization unit based on the LCO-FLL. The cascade and parallel LCO-FLL structures are described in Section III. Experimental results are presented and discussed in Section IV. Finally, conclusions are drawn in Section V.

II. Problem Formulation and Preliminary Results

A limit cycle (LC) is a closed, isolated trajectory that can arise in nonlinear dynamical systems. Depending on its stability properties, nearby trajectories may converge to or diverge from the cycle. In the case of a stable (attractive) limit cycle, trajectories in its basin of attraction asymptotically approach it [37].

In recent years, control strategies exploiting limit cycle behavior have gained attention due to their inherent stability and robustness properties [38]. In particular, stable limit cycles exhibit resilience to unmodeled dynamics and external disturbances, which enhances their applicability in practical control scenarios [30].

In this work, we consider a specific oscillator model whose dynamics, expressed in polar coordinates, are given by:

$$\dot{a} = \left[\kappa_v \epsilon_v \sin(\theta_o) + a - \frac{a^3}{A_p^2}\right]\omega, \tag{1a}$$

$$\dot{\theta}_o = \frac{-\left(a - \kappa_v \epsilon_v \cos(\theta_o)\right)}{a}\omega, \tag{1b}$$

$$\dot{\delta} = -\kappa_f a \epsilon_v \cos(\theta_o), \tag{1c}$$

where ϵ_v denotes the error signal, defined as $\epsilon_v := u - a\sin(\theta_o)$; A_p denotes the amplitude of a, i.e., $A_p := \max_{t\in\mathbb{R}} a$; the natural frequency ω is defined as $\omega := \delta + \bar{\omega}$, with $\bar{\omega}$ a real value fixed at the nominal grid frequency ($2\pi 50$ rad/s); κ_v, κ_f are real constants; and the variable δ represents the frequency adaptation, which compensates the frequency deviations. Furthermore, for the purpose of dynamic analysis, the input signal $u(t)$ is initially assumed to be an undisturbed sinusoidal waveform, defined as:

$$u = A_p^{'} \sin\left(\bar{\theta}_{ref}\right), \tag{2}$$

with $\bar{\theta}_{ref} = \bar{\omega}_{ref} t$ as the reference phase, and $\bar{\omega}_{ref}$ denoting the reference natural frequency.

However, practical grid voltages are rarely purely sinusoidal and often contain harmonic and interharmonic distortions. Therefore, a more realistic representation of the input signal is considered by modeling the grid voltage as the sum of its spectral components according to

$$v_{in} = \sum_{i=1}^{\infty} A_i \sin(2\pi f_i t + \phi_i), \tag{3}$$

where A_i, f_i, and ϕ_i correspond to the amplitude, frequency, and phase of the i-th component, respectively. Accordingly, this work aims to propose a set of enhancement multiple LCO–FLL topologies that enable the real-time detection and isolation of the amplitude, frequency, and phase parameters (A_i, ω_i, ϕ_i) of each component i present in the input signal v_{in}.

Based on stability analysis, convergence proofs, and both simulation and experimental results, previous studies such as [30] have shown that the trajectory a converges to the reference signal in (2), preserving the angular frequency $\bar{\omega}_{ref}$ and phase θ_{ref}. The mechanism to reach the natural frequency $\bar{\omega}_{ref}$ is done by (1c), which has been reported as a robust structure against frequency disturbances and adaptability [32].

For a more intuitive visualization, the dynamic behaviour of system (1) is represented in a three-dimensional state-space plot, as shown in Fig. 2(a). In this figure, the blue circle at the base represents the trajectory of (1a), which is defined with a circle with a diameter of $2A_p$. Moreover, any other trajectory (shown in green), whether initiated in or out of this circle, will at last converge toward the trajectory in blue with a frequency ω. Consequently, it can be verified that Eq.(1) admits an attractive closed orbit.

Limit Cycle Existence Verification.

Eq. (1) is a continuously differentiable vector field and around $a = A_p$ does not have any fixed point, as it can be seen graphically in Fig. 2(a). In addition, any trajectory with an initial radius $\hat{a} < A_p$ evolves outward toward $a = A_p$, since the vector field satisfies $\dot{a} > 0$ in Eq. (1). Conversely, trajectories starting at $\hat{a} > A_p$ move inward toward the same radius, driven by the condition $\dot{a} < 0$. This can be verified by analysing the sign of $\frac{d\dot{a}}{da}$ in Eq. (1a) around the trajectory when $\hat{a} = A_p \pm \Delta_a$, with Δ_a as a small deviation from A_p, this is:

$$\frac{d\dot{a}(t))}{da}_{\hat{a}=A_p\pm\Delta_a} = \left(\kappa_v sin^2(\theta_o) + 1 - 3\frac{\hat{a}^2}{A_p^2}\right)\omega, \quad (4)$$

with the subset $R = \{\hat{a} = A_p \pm \Delta_a \in \mathbb{R}^+\}$. Taking the maximum value of $sin^2(\theta_o) = 1$, and a trajectory starting at $\hat{a} > A_p$ ($\hat{a} = A_p + \Delta_a$); Eq. (4) turns to:

$$\frac{d\dot{a}(t))}{da}_{\hat{a}=A_p+\Delta_a} = \left(\kappa_v - 2 - 6\frac{\Delta_a}{A_p} - 3\frac{\Delta_a^2}{A_p^2}\right)\omega \quad (5)$$

Eq. (5) is negative if the next inequality remains:

$$2 + 6\frac{\Delta_a}{A_p} + 3\frac{\Delta_a^2}{A_p^2} > \kappa_v \quad (6)$$

In the case when the trajectory of Eq. (1a) is near to the input signal u, this is when $\epsilon_v \approx 0$, Eq. (6) turns to:

$$2 + 6\frac{\Delta_a}{A_p} + 3\frac{\Delta_a^2}{A_p^2} > 0, \quad (7)$$

and Eq. (7) is satisfied in all the time.

On the other hand, for a trajectory starting at $\hat{a} < A_p$; ($\hat{a} = A_p - \Delta_a$), Eq. (4) turns to:

$$\frac{d\dot{a}(t))}{da}_{\hat{a}=A_p-\Delta_a} = \left(\kappa_v - 2 + 6\frac{\Delta_a}{A_p} - 3\frac{\Delta_a^2}{A_p^2}\right)\omega \quad (8)$$

Hence, Eq. (8) can be positive just when:

$$2 - 6\frac{\Delta_a}{A_p} + 3\frac{\Delta_a^2}{A_p^2} < \kappa_v \quad (9)$$

It is highlighted that Eq. (9) always fulfills when the rate of Δ_a/A_p is between $[1 - 1/\sqrt{3}, 1 + 1/\sqrt{3}]$. Also, when the trajectory of the Eq. (1a) is near to the input u ($\epsilon_v \approx 0$), Eq. (9) turns to:

$$2 - 6\frac{\Delta_a}{A_p} + 3\frac{\Delta_a^2}{A_p^2} < 0, \quad (10)$$

and it is positive when $0 < \Delta_a < \left(1 - \frac{1}{\sqrt{3}}\right) A_p$.

Hence, the dynamic convergence to $a = A_p$ in a subset around A_p, establishes this radius as an attracting set

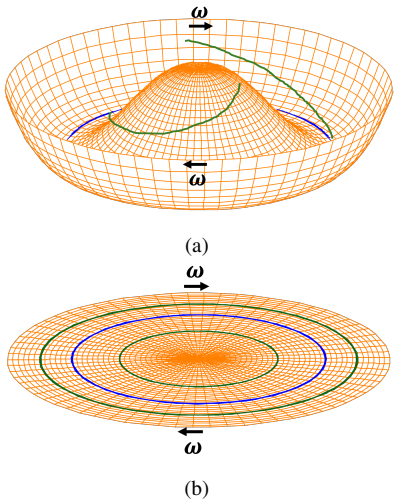


Fig. 2. Comparison between a nonlinear LCO and a linear oscillator. (a) LCO 3D representation. The green trajectories illustrate the convergence from different initial conditions toward the limit cycle, while the closed orbit of radius $r = A_p$ is shown in blue. (b) Linear oscillator flattened representation. The green path depict the system response from selected initial conditions, and the blue curve corresponds to the orbit of radius $r = A_p$.

in Eq. (1). Consequently, the solution evolves with angular velocity ω, and it constitutes an attractive Closed Orbit in Eq. (12) at the trajectory with radius A_p.

Limit Cycle Oscillator Cartesian Representation.

The set of equations presented in (1) can be reformulated through a transformation into Cartesian coordinates (See Appendix for a detailed description of the transformation). This approach provides an alternative representation that facilitates the analysis of the system dynamics. The resulting expressions are given as follows:

$$a := \|\boldsymbol{x}\|, \quad (11a)$$
$$x_1 := \cos(\theta_o)a, \quad (11b)$$
$$x_2 := \sin(\theta_o)a, \quad (11c)$$

where $\boldsymbol{x} := [x_1\, x_2]^T$. Thus,

$$\dot{x_1} = \left[x_1 + x_2 - \frac{x_1^2 + x_2^2}{A_p^2}x_1\right]\omega, \quad (12a)$$
$$\dot{x_2} = \left[-x_1 + x_2 - \frac{x_1^2 + x_2^2}{A_p^2}x_2\right]\omega + \kappa_v\epsilon_v\omega, \quad (12b)$$
$$\dot{\delta} = -x_1\kappa_f\epsilon_v, \quad (12c)$$

It can be readily observed from Eq. (12) that the dynamics of the LCO are represented in a two-dimensional plane, as described by the first expression of Eqs. (12a) and (12b). Furthermore, Eq. (12c) reveals that the FLL is governed by the error signal ϵ_v and the 90 lag signal x_1. The coupling between the FLL and the LCO is explicitly established in the last expression of Eq. (12b), highlighting, in this sense, interconnection between both subsystems.

Comparison of the LCO versus a Linear Oscillator.

The response characteristics of LC differ fundamentally from those observed in systems with linear equations. One

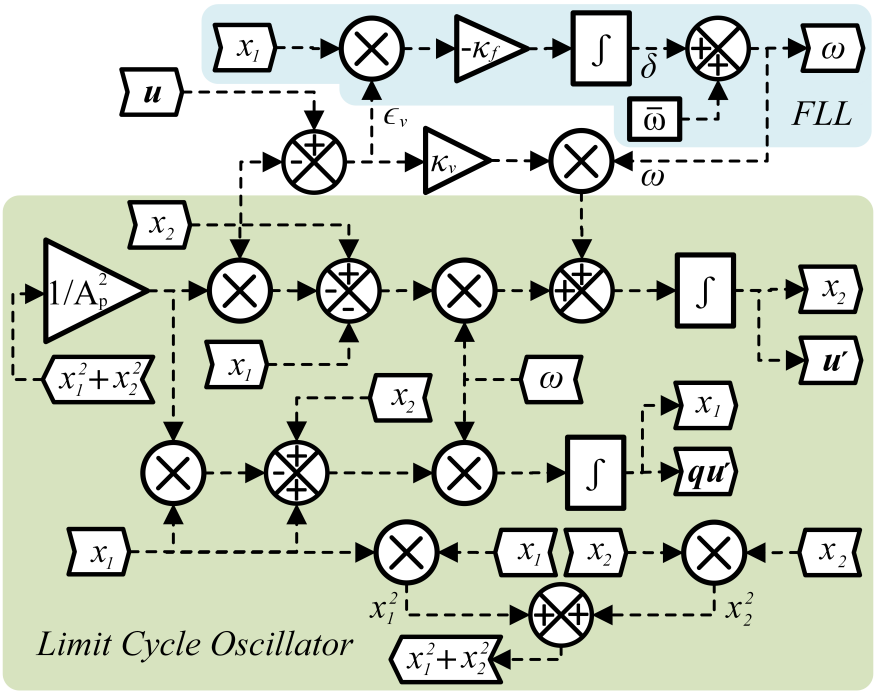


Fig. 3. Block diagram of the LCO-FLL scheme. The Limit Cycle Oscillator (LCO), highlighted by the green shaded area, is composed of six multipliers, four summing junctions, and two integrators. The Frequency-Locked Loop (FLL), highlighted by the blue shaded area, consists of one multiplier, one summing junction, and one integrator.

example can be a linear oscillator which has a flattened behaviour depicted in Fig. 2(b). This graphic has a distinct response compared to nonlinear dynamics. In contrast, the properties of Limit Cycle Oscillators (LCOs) are particularly well suited for the detection of oscillatory components within signals, such as harmonics, making them a valuable tool in advanced control applications.

Therefore, the expressions $\kappa_v \epsilon_v \omega$ in Eqs. (12b), and $x_1 \kappa_f \epsilon_v$ in (12c) vanish when the error ϵ_v becomes zero. Consequently, the LCO - FLL behaves equivalently to a conventional LCO, once the frequency signal is predicted correctly [30].

As can be seen in Fig. 3, the representation of the LCO - FLL is depicted; hence, the LCO is highlighted in green, while the FLL is shown in blue. Both subsystems are interconnected and operate in synchrony. The overall system receives the input signal u and provides the quadrature component output $qu^{'} = x_1$, and the main output $u^{'} = x_2$, which remains synchronized with the signal u. Then, it should be noted in Eq. (12) that the parameter A_p is constant; as a result, the LCO-FLL is capable of maintaining proper operation even with severe disturbances in the grid. As a result, this property contributes to the robustness of the structure under voltage fluctuations [30].

III. Interconnecting LCO-FLLs

The following proposed approaches are based on the interconnection of multiple LCO-FLL blocks, exploiting the property that each block synchronizes with a single sinusoidal component of the input signal. Consequently, once the i-th LCO-FLL synchronizes with a component of the perturbed input signal, its state variables directly provide estimates of the corresponding signal parameters, namely the amplitude A_k, the angular frequency ω_k, and the phase $\theta_k(t)$. Two fundamental architectures can be derived from this principle: the cascade interconnection and the parallel interconnection of LCO-FLL blocks. These topologies constitute the basic configurations for the extraction and estimation of multiple signal components.

A. Cascade Interconnection of LCOs

Fig. 4 illustrates an alternative configuration of the cascade interconnection of LCO-FLL units from [36]. In this structure, each LCO-FLL is represented as a separate block. Therefore, each block is synchronised with the main input v_{in} at the fundamental frequency. Hence, the signal v_{1f} is denoted as the output of the first block. By subtracting this synchronized signal v_{1f} from the original input v_{in}, a new error signal ε_1 is obtained. In steady-state conditions, ε_1 no longer contains the signal with the smallest frequency v_{1f}. Then, the signal ε_1 is utilised as input by a subsequent block of LCO-FLL, which generates the synchronized output v_{2f}. As in the first stage, subtracting v_{2f} from ε_1 produces a new error signal that can be processed by additional LCO-FLL units.

In other words, the error signal ε_{k-1} acts as a natural filtering mechanism that suppresses the previously detected low-frequency components, thereby enabling the subsequent LCO-FLL to synchronize with the next dominant harmonic/inter-harmonic. This iterative procedure can be extended as many times as required to detect harmonics and inter-harmonics. Consequently, Fig. 4 shows that the synchronized signals $v_{1f}, v_{2f}, \ldots, v_{nf}$ can be extracted, encompassing the funda-

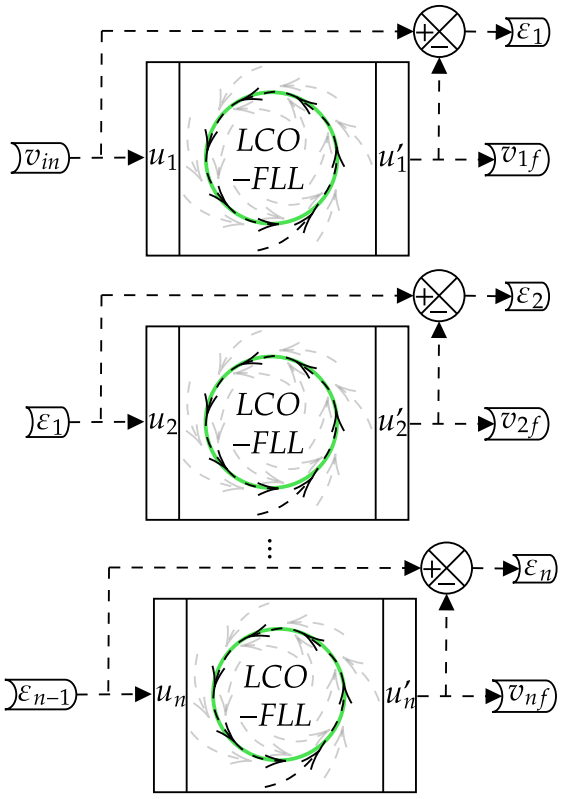


Fig. 4. Cascade interconnection of LCO-FLL units, illustrating the sequential structure employed to extract the fundamental component, harmonics, and inter-harmonics from the input signal.

mental component, harmonics, and inter-harmonics present in v_{in}.

B. Parallel Connection of LCO-FLLs

The block scheme in Fig. 5 depicts the suggested harmonic and inter-harmonic detection configuration, using a parallel connection of LCO-FLLs. The configuration presented herein represents an advancement over the topology proposed in [35], as each block of the parallel topology has now been designed as a fully integrated LCO-FLL structure, rather than consisting solely of LCO blocks dedicated to detecting harmonic components. With this modification, the architecture is also capable of detecting inter-harmonic components. This architectural refinement endows the synchronization framework with several enhanced features—outlined in the following sections—that distinguish it from the earlier parallel configuration, both in terms of performance and adaptability.

The harmonics/inter-harmonics detector consists of n LCO-FLL synchronisation blocks. Every nonlinear LCO-FLL block has as input the voltage v_{in}, and they work all together in a parallel configuration. This implies that the system must incorporate several LCO-FLL blocks equal to the inter-harmonics and harmonics to be detected. In other words, each block is responsible for synchronizing with and extracting a specific frequency component, ensuring that the overall architecture can identify both harmonic and inter-harmonic contributions present in the input signal.

The diagram in Fig. 5 illustrates the parallel configuration of LCO-FLL units, where all frequency components—including the fundamental, harmonics, and inter-harmonics are synchronised. In this structure, the upper LCO-FLL block is tuned to the fundamental component, while the remaining blocks are adjusted to higher-order harmonic or inter-harmonic frequencies. To accelerate the detection process, each LCO-FLL subtracts the perturbations identified by the other oscillators, thereby isolating its corresponding frequency component.

Indeed, the internal states of each oscillator (the amplitude a, the adapted frequency ω, and the phase θ_o) are precisely the real-time predictions of these parameters. This mechanism is depicted in Fig. 5. Formally, the input signal of the j-th block can be expressed as:

$$v_{j,in} = v_{in} - \sum_{i\neq j;i=1}^{n} v_{i,out} \tag{13}$$

for any harmonic or inter-harmonic j, as well as the fundamental signal. This formulation highlights the cooperative nature of the parallel LCO-FLL architecture, enabling simultaneous extraction of multiple frequency components from the input signal.

IV. Experimental Results

The detection block diagrams were experimentally validated at the Smart Energy Integration Laboratory (SEIL) of IMDEA Energy, Madrid, Spain (see Fig. 6(a)). In this setup, a polluted grid containing multiple inter-harmonic components was emulated through a 75 kVA Voltage Source Converter (VSC). Additionally, a second VSC rated at 15 kVA and operating with a sampling frequency of 10 kHz was employed to measure the grid voltage and to implement the proposed harmonic and inter-harmonic detection system in a Fanless Industrial Computer NEXCOM NISE 3140.

Fig. 6 (b) depicts the diagram of the experimental setup. Measurements of the three-phase voltage sensors (v_{abc}) are used as inputs for the Cascade and Parallel LCO-FLL topology detectors to identify the different frequencies present in the input signal. Therefore, three different inter-harmonics were added to the 50 Hz fundamental grid signal. Table I summarizes the frequencies, amplitudes, and phases of the sinusoidal components that constitute the input voltage signal, expressed as:

$$v_{in,4} = \sum_{i=1}^{4} A_i sin(2\pi f_i t + \phi_i) \tag{14}$$

It is worth noting that the maximum value assigned to the trajectory radius a was deliberately selected according to the overvoltage protection threshold of the experimental setup. Once this limit is reached, the protection mechanism automatically disconnects the electrical circuit, thereby preventing potential damage to the system. Considering the worst-case operating condition, the trajectory radius is bounded by $(3/2)A_p$, which corresponds to 150% of the maximum amplitude. According to [30], the optimal value for the gain

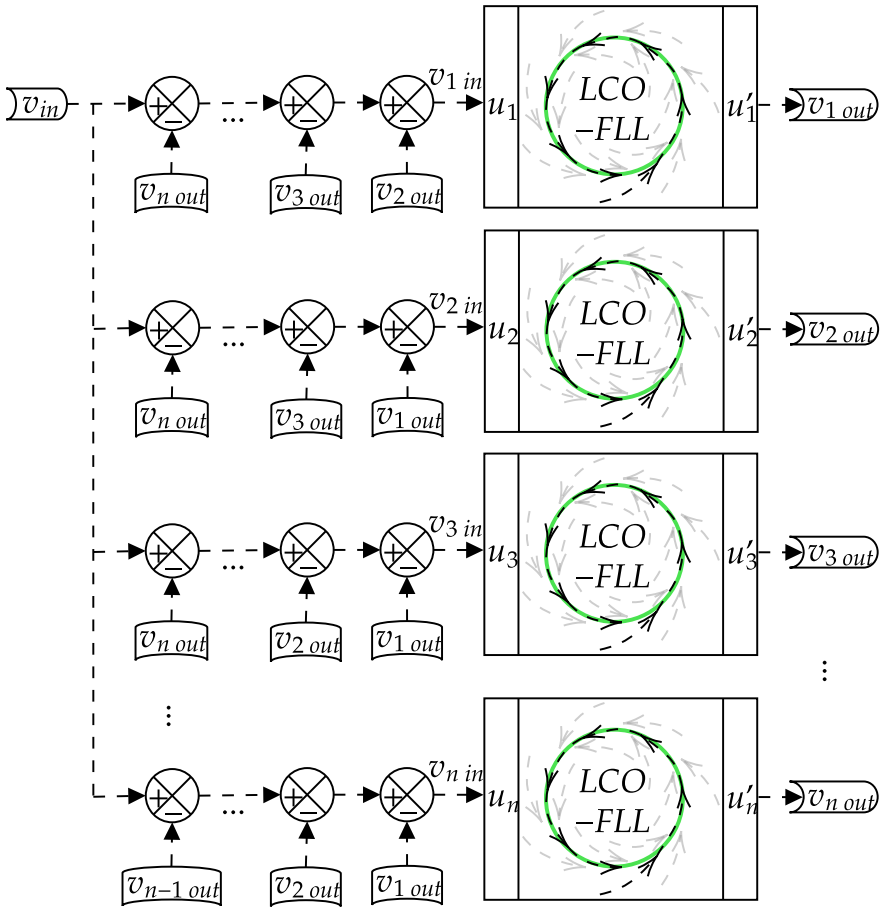


Fig. 5. Block diagram of the harmonic and inter-harmonic detection scheme, implemented through parallel-connected LCO-FLL units. This configuration enables the simultaneous extraction of all the signals components, including inter-harmonics, harmonics, and the fundamental component that is built the main signal v_{in}.

TABLE I
HARMONIC AND INTER-HARMONIC COMPONENTS USED FOR THE TESTS

Harmonic/ Inter-harmonics*	Frequency (Hz)	Amplitude (V)	Phase (rad)
1	$f_1 = 50$	$A_1 = 165$	$\phi_1 = 0$
–	$f_2 = 249$	$A_2 = 50$	$\phi_2 = -\pi/3$
–	$f_3 = 539.15$	$A_3 = 25$	$\phi_3 = -2\pi/3$
–	$f_4 = 778$	$A_4 = 15$	$\phi_4 = \pi/3$

* Steady-state voltage regulation of the 75-kVA VSC: $\pm 1\%$.

κ_v yields to κ_v=13/4. In addition, the gain κ_f was assigned the optimized value reported in [30], namely κ_f=5. Therefore, both topologies have been set with the same parameters for comparison purposes.

As it can be seen in Fig. 7, the Cascade and the Parallel LCO-FLLs topologies take different settling times in the process of identifying the first harmonic and the three different inter-harmonics present in the input signal. For the first harmonic (50 Hz), the Cascade topology takes 475 ms to settle the final frequency, however, the Parallel topology takes 300 ms to identify the signal, this corresponds to a 175-ms reduction in the detection time compared with the cascade topology.

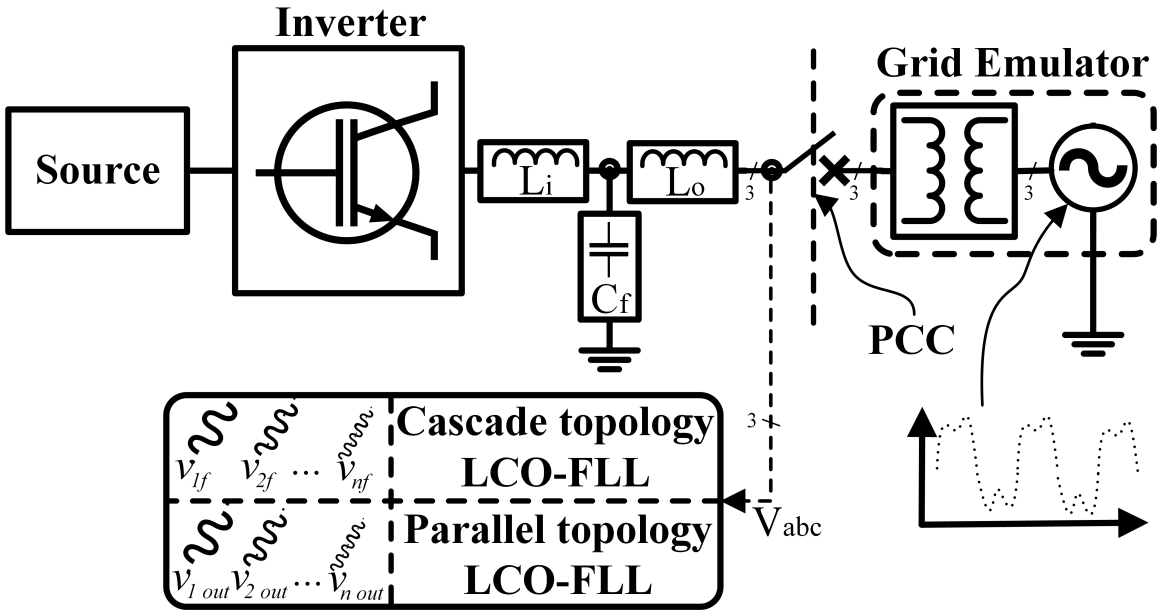
Afterwards, the Cascade topology takes 900 ms to identify the inter-harmonic 249 Hz. In contrast, the Parallel topology takes just 500 ms to detect the signal, which makes it almost twice as fast as the Cascade topology.

Furthermore, the Cascade topology detects the non integer inter-harmonic 539.15 Hz in 300 ms. Nevertheless, the Parallel topology identifies the same signal in half the time, in 150 ms. Finally, the Cascade topology detects the inter-harmonic 778 Hz in 200 ms. However, the Parallel topology identifies it in just 75 ms, which is three times faster than the Cascade topology.

The comparison of detection times for Cascade and Parallel topologies is summarized in Table II. It can be seen that the Parallel topology has faster detection times than the Cascade topology. This fact can be attributed to the arrangement connection of the LCO-FLL blocks, as in the parallel topology, every block processes the signal in parallel. Meanwhile, in the Cascade connection, the data processing is in series, resulting in a longer processing time compared to the Parallel connection.



(a)



(b)

Fig. 6. (a) 1) Laboratory overview, 2) 15 kVA VSCs, 3) 75 kVA VSCs, 4) real-time Fanless Industrial Computer NEXCOM NISE 3140 and 5) external computers. (b) Experimental setup.

Both architectures operate without requiring prior knowledge of the number of harmonic or inter-harmonic components present in the signal. If an unexpected frequency component arises in the input, it manifests as a perturbation in the detected signal associated with the highest frequency, namely in the output of the last LCO-FLL block in both topologies. In practice, the detection process proceeds sequentially from the slowest (lowest frequency) to the fastest (highest frequency) signals. When the number of components exceeds the available LCO-FLL blocks, the additional components appear as perturbations in the output of the block corresponding to the largest frequency.

A. Steady State Signals Comparison

After analyzing the transient stage of the different detected signals, it is crucial to compare the dynamic behaviour of the identified signals in the steady state. Fig. 8 shows in blue line, the input voltage signal v_{in}, which has all the signal distortions (Harmonic and inter-harmonics) summarized in Table I. Moreover, it shows the fundamental voltages detected

TABLE II
COMPARISON OF DETECTION TIMES OF CASCADE AND PARALLEL TOPOLOGIES

Harmonic/ Inter-harmonics	Frequency (Hz)	Cascade Topology Detection Time (ms)*	Parallel Topology Detection Time (ms)*
1	50	475	300
–	249	900	500
–	539.15	300	150
–	778	200	75

* Optimized parameters: $\kappa_v = 3.25$ and $\kappa_f = 5$, as reported in [30].

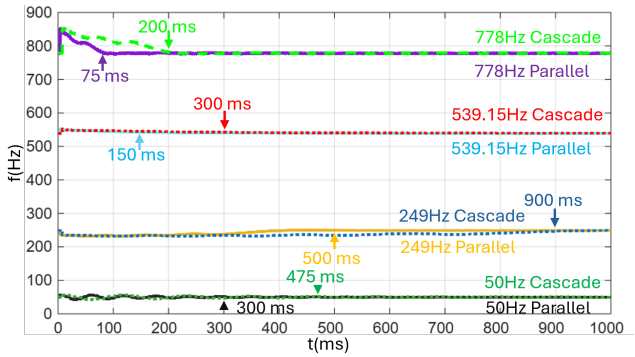


Fig. 7. Frequency signals detected by the Cascade and the Parallel LCO-FLLs topologies.

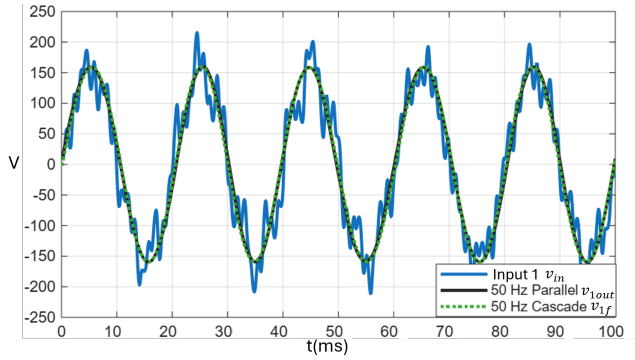


Fig. 8. Input voltage v_{in} with harmonics and inter-harmonics (Blue line for Parallel and Cascade topology). Fundamental voltages detected by Parallel v_{1out} (Black line) and Cascade topology v_{1f} (Green dotted line).

by the Parallel topology v_{1out} in black line, and the signal detected by the Cascade topology v_{1f} represented by the green dotted line. It can be seen that both detected signals have almost identical frequencies and phases, since it is the fundamental frequency of the input signal.

It is relevant to highlight in the Cascade topology (Fig. 4) that the error signal computed by the first LCO-FLL block $\varepsilon_1 = v_{in} - v_{f1}$ is the input of the second LCO - FLL block, which can be compared with the input signal of the second LCO - FLL of the Parallel topology v_{2in}, defined as:

$$v_{2in} = v_{in} - v_{1out} - v_{3out} - v_{4out} \tag{15}$$

Therefore, both input signals, v_{in2} and ε_1 are used as input signals for the second LCO-FLL blocks of both topologies.

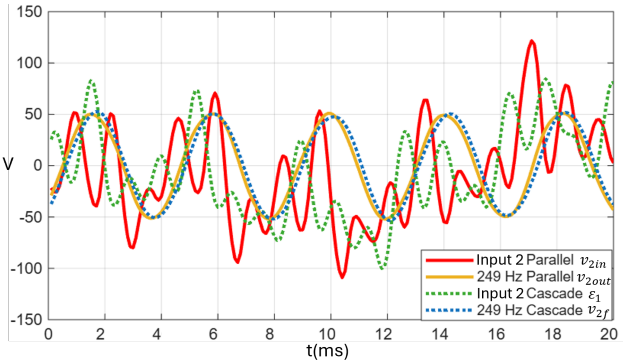


Fig. 9. Input voltages v_{2in} in red line for parallel topology, and error signal ε_1 in green dotted line for Cascade topology ($\varepsilon_1 = v_{in} - v_{f1}$). Inter-harmonic detected 249 Hz by Parallel v_{2out} (Orange line) and Cascade topology v_{2f} (Blue dotted line).

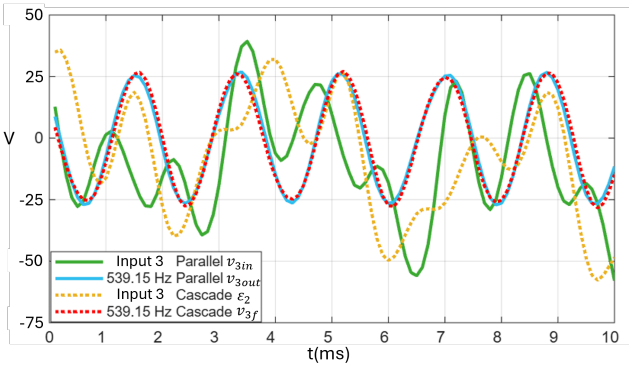


Fig. 10. Input voltages v_{3in} in green line for Parallel topology and Orange dotted line ε_2 for Cascade topology ($\varepsilon_2 = \varepsilon_1 - v_{2f}$). Inter-harmonic 539.15 Hz detected by Parallel v_{3out} (Blue line) and Cascade topology v_{3f} (Red dotted line).

Hence, in Fig. 9, v_{2in} (Red line) and ε_1 (Green dotted line), are the second input for both topologies (Parallel and Cascade). It can be seen that they have similar dynamics but different trajectories due to different process methods. Consequently, the Parallel and Cascade topologies detect the 249 HZ inter-harmonic signal, which can be seen in Fig. 9 as Orange line v_{2out} and Blue dotted line v_{2f}, respectively. Note that there is a slight phase difference between both inter-harmonic detections.

In order to detect the non integer inter-harmonic 539.15 Hz, the third LCO-FLL block is used in both topologies (Parallel and Cascade). Thus, the input 3 for the parallel topology is processed and is given by:

$$v_{3in} = v_{in} - v_{1out} - v_{2out} - v_{4out} \tag{16}$$

On the other hand, the input 3 for the Cascade topology is given by $\varepsilon_2 = \varepsilon_1 - v_{2f}$ according to Fig. 4.

As a result, the inter-harmonic 539.15 Hz is detected by the parallel topology and depicted in Fig. 10 in blue line v_{3in}. In addition, the cascade topology detects the same inter-harmonic and presented in red dotted line v_{3f}. Both detected signals remain with almost no phase changes during the steady state time.

Finally, it was implemented a fourth LCO-FLL block to detect the inter-harmonic 778 Hz in both topologies. The Input 4 for the parallel topology v_{4in} is depicted in Fig. 11 in dark blue line, and is given by:

$$v_{4in} = v_{in} - v_{1out} - v_{2out} - v_{3out} \tag{17}$$

And the Input 4 for the Cascade topology is presented in a yellow dotted line, and defined as $\varepsilon_3 = \varepsilon_2 - v_{3f}$.

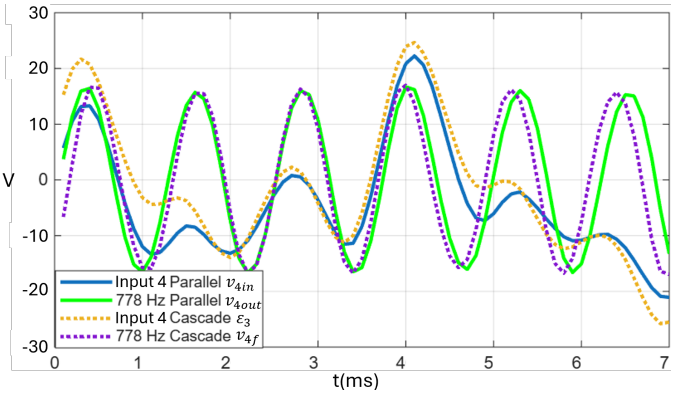


Fig. 11. Input voltages v_{4in} in dark blue line for Parallel topology and yellow dotted line ε_3 for Cascade topology ($\varepsilon_3 = \varepsilon_2 - v_{3f}$). Inter-harmonic 778 Hz detected by Parallel v_{4out} (Green line) and Cascade topology v_{4f} (Purple dotted line).

The Parallel topology detects the inter-harmonic 778 Hz, and it is shown in green line in Fig. 11. Also, the Cascade topology detects the same inter-harmonic, as presented by the purple dotted line in Fig. 11. In this Inter-harmonic, a small phase drift can be observed between both detected signals. However, it is small enough, since both signals remain in steady state.

Finally, it is important to highlight that assigning gains of κ_v and κ_f above the values indicated leads to oscillations around a fixed value in the steady-state signals of frequency and phase. Conversely, selecting values lower than those reported in the footnote of Table II may result in the loss of frequency signals and prevent convergence to any fixed value.

B. Tecnical Data of Steady-state Errors and Comparative Performance Between Cascade and Parallel Topologies

Table III summarizes the most relevant results obtained in the comparative analysis between cascade and parallel topologies. The evaluation considers steady-state errors in frequency, magnitude, and phase, as well as computational performance metrics such as scan time, processor load, RAM consumption, and jitter. This comparative framework provides a comprehensive view of the trade-offs between both configurations.

a) Steady-State Errors:

- **Frequency Error:** The maximum variation in frequency was consistently lower for the parallel topology. For the first signal, the error was ± 0.16 Hz in cascade and ± 0.13 Hz in parallel. For the second signal, the values were ± 0.68 Hz (cascade) and ± 0.56 Hz (parallel). The third signal showed ± 1.63 Hz (cascade) versus ± 1.26 Hz (parallel), while the fourth signal reached ± 2.14 Hz (cascade) compared to ± 1.97 Hz (parallel). These results indicate that the parallel configuration achieves slightly improved frequency tracking accuracy across all signals.
- **Magnitude Error:** The maximum variation in magnitude remained nearly identical between both topologies. For the first signal, both cascade and parallel exhibited 1.2%. The second signal showed 4% (cascade) and 3.9% (parallel). The third and fourth signals presented equal values in both configurations (7% and 6.6%, respectively). This suggests that magnitude estimation is robust and largely independent of the chosen topology.
- **Phase Error:** The parallel topology demonstrated a clear advantage in phase accuracy. For the first signal, both topologies yielded ± 0.1 rad. However, for the second signal, the cascade error was ± 0.63 rad compared to ± 0.31 rad in parallel. Similarly, the third signal showed ± 0.67 rad (cascade) versus ± 0.34 rad (parallel). The fourth signal presented the largest discrepancy, with ± 1.9 rad in cascade and ± 0.9 rad in parallel. These results confirm that the parallel configuration provides more precise phase estimation, particularly for higher-order signals.

b) Performance of the Fanless Industrial Computer NEXCOM NISE 3140: The experimental implementation was carried out on a fanless industrial computer NEXCOM NISE 3140, and the following aspects were observed:

- **Scan Time:** The total time required for reading inputs, executing program instructions, and updating outputs was fixed at 100 μs for both topologies.
- **Processor Load (Central Processing Unit-CPU Usage):** The parallel topology required 14.7% of processor capacity, whereas the cascade topology consumed only 3.4%. This indicates that the parallel configuration demands approximately 4.3 times more CPU usage, mainly due to simultaneous mathematical operations involving text variables and floating-point numbers.
- **RAM Consumption:** The parallel topology occupied 5.31 Mb of memory, while the cascade topology required 4.23 Mb. The difference (about 1.25 times higher in parallel) is relatively small, as both implementations avoid storing static data during execution.
- **Jitter:** When communicating with external hardware via Ethernet, the worst-case jitter was 43 μs for the cascade topology and 17 μs for the parallel topology. This means that the parallel configuration achieves approximately 2.5 times lower jitter, which is consistent with the faster response of the LCO-FLL in both topologies (around 2.66 for the fourth signal).

Overall, the comparative analysis reveals that the parallel topology achieves lower steady-state errors in both frequency and phase, while magnitude errors remain nearly identical across configurations. In addition, the parallel approach provides reduced jitter and improved synchronization performance, reinforcing its accuracy in dynamic tracking. However, these benefits come at the cost of significantly higher processor load, as the parallel implementation demands greater compu-

TABLE III
SUMMARY OF THE MOST RELEVANT RESULTS OBTAINED IN THE COMPARATIVE ANALYSIS BETWEEN CASCADE AND PARALLEL TOPOLOGIES

Topology	Cascade	Parallel
Frequency Steady-State Error (Maximum Frequency Variation)		
1◇ Signal	±0.16 Hz	±0.13 Hz
2♦ Signal	±0.68 Hz	±0.56 Hz
3▲ Signal	±1.63 Hz	±1.26 Hz
4° Signal	±2.14 Hz	±1.97 Hz
Magnitude Steady-State Error (Maximum Magnitude Variation)		
1◇ Signal	1.2%	1.2%
2♦ Signal	4.0%	3.9%
3▲ Signal	7.0%	7.0%
4° Signal	6.6%	6.6%
Phase Steady-State Error (Maximum Phase Variation)		
1◇ Signal	±0.1 rad	±0.1 rad
2♦ Signal	±0.63 rad	±0.31 rad
3▲ Signal	±0.67 rad	±0.34 rad
4° Signal	±1.9 rad	±0.9 rad
Implementation Metrics		
Scan Time*	100 μs (Fixed)	100 μs (Fixed)
Processor Load*	3.4%	14.7%
RAM Consumption*	4.23 MB	5.31 MB
Jitter (Worst Case)*	43 μs	17 μs

◇ 50 Hz signal. ♦ 249 Hz signal. ▲ 539.15 Hz signal. ° 778 Hz signal.
* Fanless industrial computer NEXCOM NISE 3140.

tational resources. Conversely, the cascade topology demonstrates lower CPU usage and reduced memory consumption, maintaining comparable performance in magnitude estimation with more efficient resource utilization. This balance highlights the importance of selecting the appropriate configuration depending on application requirements: the parallel topology offers superior tracking precision, while the cascade topology ensures computational efficiency.

C. Comparison with Established Detection Methodologies

To evaluate the operational efficacy of established spectral estimation techniques versus LCO-FLL-based models under inter-harmonic conditions, a comparative performance analysis was conducted. Table IV details the specific trade-offs inherent to each architectural paradigm across three critical performance vectors: estimation accuracy, convergence latency, and computational complexity.

V. CONCLUSION

In this paper, two enhancement methods for detecting harmonics and inter-harmonics in power systems have been compared experimentally. These methods are based on interconnected LCO-FLLs blocks in a cascade and parallel configuration. In the cascade topology, the remaining components to be identified are obtained by successively subtracting the computed signals from the main input. Conversely, in the parallel configuration, the output of each block of LCO-FLL is subtracted from the input of the other units, thereby enhancing the overall accuracy of the detection process.

The transient responses obtained by the parallel topology exhibited a relative fast dynamic behavior, demonstrating the efficiency of the proposed system during non-steady-state conditions. Therefore, the parallel topology is faster than the cascade topology, since in the parallel topology, every block processes the signal in parallel. Meanwhile, in the Cascade connection, the data process is in series, resulting in a longer processing time compared to the Parallel connection. This capability comes at the cost of greater computational effort, since all branches in the parallel model operate simultaneously and require additional processing power.

Experimental results have demonstrated that the proposed configurations are effective for estimating voltage harmonics/inter-harmonics, thereby enabling fault diagnosis. As part of future work, these methods could be extended to electric machines for grid monitoring and diagnostic purposes, enabling the detection of harmonics and inter-harmonics on currents and voltages even under rapid frequency variations. Such extension is expected to contribute to improving reliability and robustness in advanced power system applications, while also offering potential benefits in terms of energy efficiency.

Finally, it is acknowledged that the settling time tends to increase with the number of components to be detected. However, this limitation can be alleviated by segmenting the frequency ranges and employing multiple topologies, depending on the signal requirements. These strategies represent promising directions for future research.

ACKNOWLEDGMENTS

The authors gratefully acknowledge the support provided to E. Vazquez and C.-F. Méndez-Barrios by the Secretariat of Science, Humanities, Technology and Innovation (SECIHTI) under Grant No. 423695. In addition, the authors extend their appreciation to IMDEA Energy for granting access to the Smart Energy Integration Lab (SEIL), which enabled the execution of the experimental tests.

APPENDIX
TRANSFORMATION FROM EQS. (1) TO EQS. (12)
DERIVATION OF STATE EQUATIONS

Differentiating Eq. (11b) yields:

$$\dot{x}_1 = \frac{\partial x_1}{\partial a}\frac{da}{dt} + \frac{\partial x_1}{\partial \theta_o}\frac{d\theta_o}{dt}, \tag{18}$$

where $\frac{da}{dt} = \dot{a}$ is given by Eq. (1a), and $\frac{d\theta_o}{dt} = \dot{\theta}_o$ is given by Eq. (1b). Substituting these expressions into Eq. (18) leads to:

$$\begin{aligned}\dot{x}_1 = \cos(\theta_o)\left[\kappa_v \epsilon_v \sin(\theta_o) + a - \frac{a^3}{A_p^2}\right]\omega \\ - a\sin(\theta_o)\left[\frac{\omega \kappa_v \epsilon_v \cos(\theta_o)}{a} - \omega\right].\end{aligned} \tag{19}$$

After simplification, and using Eqs. (11b) and (11c), Eq. (19) reduces to Eq. (12a). Similarly, differentiating Eq. (11c) yields:

$$\dot{x}_2 = \frac{\partial x_2}{\partial a}\frac{da}{dt} + \frac{\partial x_2}{\partial \theta_o}\frac{d\theta_o}{dt}, \tag{20}$$

TABLE IV
COMPARATIVE ANALYSIS OF ESTABLISHED HARMONIC AND INTER-HARMONIC DETECTION TECHNIQUES VERSUS LCO-FLL-BASED MODELS

Methodology Class	Estimation Accuracy	Dynamic Response & Convergence	Computational Complexity
Fourier-Based Methods [39]	**Highly Variable**. Demonstrates bounded precision for integer components; exhibits severe degradation via **spectral leakage** and picket-fence effects under asynchronous interharmonic sampling.	**Instantaneous**. Non-iterative execution bounded entirely by the discrete physical window parameter (e.g., standard IEC 200 ms observation interval).	**Deterministic Low**. Bounded by $(N \log N)$ complexity metrics, establishing the baseline benchmark for real-time edge processing and smart metering hardware.
Parametric High-Resolution [40]	**High**. Offers sub-Hertz spectral resolution independent of window limitations; vulnerable to numerical instability under low signal-to-noise ratios (SNR).	**Latent**. Exhibits systemic propagation delay due to the computational dependency on multi-order polynomial decomposition and matrix inversion routines.	**Severely Elevated**. Governed by Matrix Singular Value Decomposition (SVD) and polynomial rooting algorithms, traditionally restricting deployment to post-process analysis.
Adaptive Filtering [41]	**High**. Provides robust tracking and noise rejection profiles under time-varying signal distributions and fundamental frequency deviations.	**Asymptotic**. Bound to the user-defined tracking step-size; introduces a fundamental compromise between steady-state accuracy and transient response latency.	**Moderate**. Characterized by sequential time-domain vector calculations, demanding recurring iteration matrix updates per discrete time-step execution.
Time-Frequency Transforms [42]	**High (Transient Domain)**. Optimally suited for capturing non-stationary, brief interharmonic perturbations; performance is coupled to proper mother wavelet selection.	**Instantaneous**. Maps temporal-spectral fluctuations dynamically without requiring iterative stabilization or search convergence loops.	**Moderate to High**. Demands extensive memory allocations and intensive multi-scale arithmetic structures for synchrosqueezing or multi-level filter banks.
Optimization & Intelligence [43]	**Exceptional**. Demonstrates high nonlinear convergence capability for extracting highly dense, overlapping interharmonic profiles.	**Protracted**. Subject to significant computational overhead during offline optimization phases or multi-iteration metaheuristic search routines.	**Extremely High**. Neural frameworks enforce demanding hardware requirements during the training phase, while heuristic methods require parallel iteration blocks.
LCO-FLL-Based Models	**High**. They offer robust online accuracy in estimating the frequency, phase, and amplitude parameters of each signal to be detected.	**Asymptotic**. Their convergence is asymptotically determined by two parameters associated with each LCO-FLL block.	**Deterministic Low**. It is restricted by the processor's capacity to perform parallel mathematical operations and increases proportionally with the number of signals to be detected.

where $\frac{da}{dt} = \dot{a}$ is given by Eq. (1a), and $\frac{d\theta_o}{dt} = \dot{\theta}_o$ is given by Eq. (1b). Substituting these expressions into Eq. (20) leads to:

$$\begin{aligned} \dot{x}_2 = \sin(\theta_o) \left[\kappa_v \epsilon_v \sin(\theta_o) + a - \frac{a^3}{A_p^2} \right] \omega \\ + a \cos(\theta_o) \left[\frac{\omega \kappa_v \epsilon_v \cos(\theta_o)}{a} - \omega \right]. \end{aligned} \tag{21}$$

After simplification, and using Eqs. (11b) and (11c), Eq. (21) reduces to Eq. (12b). Finally, Eq. (1c) can be transformed into Eq. (12c) by substituting Eq. (11b) into Eq. (1c).

REFERENCES

[1] L. Michalec, M. Jasinski, T. Sikorski, Z. Leonowicz, L. Jasinski, V. Suresh, and L. Michalec, "Impact of harmonic currents of nonlinear loads on power quality of a low voltage network–review and case study," *Energies*, vol. 14, no. 12, 2021.

[2] O. Avalos, E. Cuevas, H. G. Becerra, J. Gálvez, S. Hinojosa, D. Zaldívar, and O. Avalos, "Kernel recursive least square approach for power system harmonic estimation," *Electric Power Components and Systems*, vol. 48, no. 16-17, pp. 1708–1721, 2020.

[3] B. Hu and H. Gharavi, "A fast recursive algorithm for spectrum tracking in power grid systems," *IEEE Transactions on Smart Grid*, vol. 10, no. 3, pp. 2882–2891, 2019.

[4] "Multi-harmonic sources identification and evaluation method based on cloud-edge-end collaboration," *International Journal of Electrical Power and Energy Systems*, vol. 156, p. 109681, 2024.

[5] ""voltage-current ratio difference" concept for identifying the dominant harmonic source," *International Journal of Electrical Power and Energy Systems*, vol. 121, p. 106147, 2020.

[6] K. Daniel, L. Kütt, M. N. Iqbal, N. Shabbir, H. A. Raja, M. U. Sardar, and K. Daniel, "A review of harmonic detection, suppression, aggregation, and estimation techniques," *Applied Sciences*, vol. 14, no. 23, 2024.

[7] C.-I. Chen and Y.-C. Chen, "Comparative study of harmonic and interharmonic estimation methods for stationary and time-varying signals," *IEEE Transactions on Industrial Electronics*, vol. 61, no. 1, pp. 397–404, 2014.

[8] M. Valtierra-Rodriguez, R. de Jesus Romero-Troncoso, R. A. Osornio-Rios, and A. Garcia-Perez, "Detection and classification of single and combined power quality disturbances using neural networks," *IEEE Transactions on Industrial Electronics*, vol. 61, no. 5, pp. 2473–2482, 2014.

[9] X. Li and W. Xu, "A novel filter to mitigate interharmonic problems caused by variable frequency drives," in *2017 IEEE 12th International Conference on Power Electronics and Drive Systems (PEDS)*, 2017, pp. 887–892.

[10] S. Jana and S. Srinivas, "A computationally efficient harmonic extraction algorithm for grid applications," *IEEE Transactions on Power Delivery*, vol. 37, no. 1, pp. 146–154, 2022.

[11] A. Bagheri, M. Mardaneh, A. Rajaei, and A. Rahideh, "Detection of grid voltage fundamental and harmonic components using kalman filter and generalized averaging method," *IEEE Transactions on Power Electronics*, vol. 31, no. 2, pp. 1064–1073, 2016.

[12] "Harmonic problems in renewable and sustainable energy systems: A comprehensive review," *Sustainable Energy Technologies and Assessments*, vol. 48, p. 101566, 2021.

[13] E. A. Bulycheva and S. A. Yanchenko, "Real-time harmonic identification under varying grid conditions," *Serbian Journal of Electrical Engineering*, vol. 18, no. 1, pp. 29–48, 2021.

[14] G. Arena, A. Chub, M. Lukianov, R. Strzelecki, D. Vinnikov, G. De Carne, and G. Arena, "A comprehensive review on dc fast charging stations for electric vehicles: Standards, power conversion

technologies, architectures, energy management, and cybersecurity," *IEEE Open Journal of Power Electronics*, vol. 5, pp. 1573–1611, 2024.
[15] S. Soliman, *Electric Power Systems Harmonics - Identification and Measurements*.
[16] A. Hoevenaars, M. Farbis, and M. McGraw, "Active harmonic mitigation: What the manufacturers don't tell you," *IEEE Industry Applications Magazine*, vol. 26, no. 5, pp. 41–51, 2020.
[17] P. Dattaray, D. Chakravorty, P. Wall, J. Yu, and V. Terzija, "A novel control strategy for subsynchronous resonance mitigation using 11 kv vfd-based auxiliary power plant loads," *IEEE Transactions on Power Delivery*, vol. 33, no. 2, pp. 728–740, 2018.
[18] "A phase compensation method combined with power correction for suppressing sub-synchronous resonance of wind generation under weak grid," *International Journal of Electrical Power and Energy Systems*, vol. 151, p. 109115, 2023.
[19] N. Verma, N. Kumar, S. Gupta, H. Malik, and F. P. García Márquez, "Review of sub-synchronous interaction in wind integrated power systems: classification, challenges, and mitigation techniques," *Protection and Control of Modern Power Systems*, vol. 8, no. 2, pp. 1–26, 2023.
[20] F. Zhang, J. Liu, W. Hu, W. Gao, and J. He, "An enhanced synchrophasor trajectory fitting technique for parameter identification of sub-/super-synchronous oscillations," *CSEE Journal of Power and Energy Systems*, pp. 1–12, 2025.
[21] IPCC, "Energy systems," in *Climate Change 2022: Mitigation of Climate Change. Contribution of Working Group III to the Sixth Assessment Report of the Intergovernmental Panel on Climate Change*, P. R. Shukla, J. Skea, R. Slade, A. Al Khourdajie, R. van Diemen, D. McCollum, M. Pathak, S. Some, P. Vyas, R. Fradera, M. Belkacemi, A. Hasija, G. Lisboa, S. Luz, and J. Malley, Eds. Cambridge, UK and New York, NY, USA: Cambridge University Press, 2022, ch. 6. [Online]. Available: https://www.ipcc.ch/report/ar6/wg3/chapter/chapter-6/
[22] D. D. A. Snehal R. Durdhavale, "A review of harmonics detection and measurement in power system," *International Journal of Computer Applications*, vol. 143, no. 10, Jun 2016.
[23] G. Carpinelli, A. Bracale, P. Varilone, T. Sikorski, P. Kostyla, Z. Leonowicz, and G. Carpinelli, "A new advanced method for an accurate assessment of harmonic and supraharmonic distortion in power system waveforms," *IEEE Access*, vol. 9, pp. 88 685–88 698, 2021.
[24] S. Shelar, D. Bankar, and S. Bakre, "Review of revisions of ieee 519 standard on power system harmonics (1981 to 2022)," pp. 415–420, 2024.
[25] Z. Zhang, S. Lu, S. Qin, B. Li, L. Ding, Z. Zhang, and S. Lu, "Harmonic measurement method and system design based on self-compensating fft," *IEEE Sensors Journal*, vol. 25, no. 13, pp. 24 588–24 597, 2025.
[26] S. Sharma, *Digital signal processing*. KHANNA PUBLISHING HOUSE, 2025.
[27] J. Enayati and Z. Moravej, "Real-time harmonic estimation using a novel hybrid technique for embedded system implementation," *International Transactions on Electrical Energy Systems*, vol. 27, no. 12, pp. 24–28.
[28] A. E. Biju, S. Srikanth, K. Manoj, S. A. Pawar, R. I. Sujith, A. E. Biju, and S. Srikanth, "Dynamics of minimal networks of limit cycle oscillators," *Nonlinear Dynamics*, vol. 112, no. 13, pp. 11 329–11 348, 2024.
[29] "Harmonics detection via input observer with grid frequency fluctuation," *International Journal of Electrical Power and Energy Systems*, vol. 115, p. 105461, 2020.
[30] E. Oviedo, N. Vázquez, and R. Femat, "Synchronization technique of grid-connected power converters based on a limit cycle oscillator," *IEEE Transactions on Industrial Electronics*, vol. 65, no. 1, pp. 709–717, 2018.
[31] R. Lautenbacher, J. Röhrig, K. Ochs, and R. Köhl, "A sufficient synchronization condition for oscillators coupled diffusively by nonlinear passive systems," *Discover Applied Sciences*, vol. 7, no. 6, p. 643, 2025.
[32] S. Golestan, J. M. Guerrero, F. Musavi, and J. C. Vasquez, "Single-phase frequency-locked loops: A comprehensive review," *IEEE Transactions on Power Electronics*, vol. 34, no. 12, pp. 11 791–11 812, 2019.
[33] Y. Zuo, X. Ge, Y. Zheng, Y. Chen, H. Wang, A. T. Woldegiorgis, and Y. Zuo, "An adaptive active disturbance rejection control strategy for speed-sensorless induction motor drives," *IEEE Transactions on Transportation Electrification*, vol. 8, no. 3, pp. 3336–3348, 2022.
[34] T. Trummel, Z. Liu, and O. Stursberg, "Analysis of synchronization errors for differently parametrized limit cycle oscillators subject to bounded disturbances," *SN Computer Science*, vol. 6, no. 7, p. 871, 2025.
[35] E. Vazquez, J. Roldan-Perez, and M. Prodanovic, "Detection of harmonics by using parallel-connected nonlinear limit cycle oscillators," pp. 70–75, 2023.
[36] E. Vazquez, J. Roldan-Perez, and M. Prodanovic, "Detection of harmonics and interharmonics by using cascaded limit cycle oscillators," pp. 1–6, 2023.
[37] S. Sastry, *Nonlinear Systems: Analysis, Stability, and Control*, ser. Interdisciplinary Applied Mathematics. New York: Springer, 1999.
[38] A. K. Verma, C. Subramanian, R. K. Jarial, and P. Roncero-Sánchez, "An enhanced discrete-time oscillator-based pll-less estimation of single-phase grid voltage parameters," *IEEE Transactions on Industrial Electronics*, vol. 69, no. 4, pp. 3977–3987, 2021.
[39] D. Gallo, R. Langella, and A. Testa, "Light flicker prediction based on voltage interharmonics assessment," *IEEE Transactions on Power Delivery*, vol. 20, no. 4, pp. 2397–2407, 2005.
[40] R. F. Brcich, Y. J. Zhang, and A. M. Zoubir, "Estimation of harmonic and interharmonic frequencies using esprit," *IEEE Transactions on Power Delivery*, vol. 24, no. 2, pp. 493–501, 2009.
[41] P. K. Dash, A. K. Pradhan, and G. Panda, "Frequency estimation of distorted power system signals using extended complex kalman filter," *IEEE Transactions on Power Delivery*, vol. 14, no. 3, pp. 761–766, 1999.
[42] S. Chandra and P. Kumar, "Detection and classification of harmonics and interharmonics using wavelet-based techniques," *IEEE Transactions on Industrial Electronics*, vol. 61, no. 8, pp. 4233–4242, 2014.
[43] W.-C. Lin and C.-H. Chen, "A hybrid neural network and particle swarm optimization approach for interharmonic parameter identification," *IEEE Transactions on Power Electronics*, vol. 34, no. 7, pp. 6124–6135, 2019.



Erick Vázquez received the B.S. degree in Electronics Engineering from the Universidad Autónoma de San Luis Potosí (UASLP), San Luis Potosí, Mexico, in 2010, and the M.Sc. and Ph.D. degrees in Control and Dynamic Systems from the Instituto Potosino de Investigación Científica y Tecnológica (IPICYT), San Luis Potosí, Mexico, in 2013 and 2019, respectively. In 2017, he was a visiting Ph.D. student at the Department of Energy Technology, Aalborg University, Denmark. From 2021 to 2023, he worked as a Postdoctoral Researcher in the Electrical Systems Unit at IMDEA Energy Institute, Madrid, Spain. In September 2025, he joined the Research and Postgraduate Studies Center of the Faculty of Engineering at the Universidad Autónoma de San Luis Potosí (UASLP) as a Postdoctoral Researcher. His main research interests include nonlinear control techniques, synchronization methods, grid-connected power converters, and anti-islanding techniques.



César Fernando Méndez-Barrios received the M.Sc. degree in control theory from the Center for Research and Advanced Studies, National Polytechnic Institute (CINVESTAV), in 2005, and the Ph.D. degree from the University of Paris-Sud XI, in 2011. Since 2012, he has been a Professor with the Mechatronics Department, Autonomous University of San Luis Potosí (UASLP). He is currently serving as an Associate Chair of the Graduate Program in Electrical Engineering. He has authored or coauthored over 30 peer-reviewed publications. His research interest belongs to the qualitative theory of dynamical systems and its application in control problems. Moreprecisely, he is interested by the qualitative analysis of the effects induced by the parameters on the systems dynamics with a particular emphasis on delays.